

A Direct Drive Parallel Plane Piezoelectric Needle Positioning Robot for MRI Guided Intraspinal Injection

Waiman Meinhold¹, Daniel Enrique Martinez, John Oshinski, Ai-Ping Hu,
and Jun Ueda², *Senior Member, IEEE*

Abstract—Recent developments in the field of cellular therapeutics have indicated the potential of stem cell injections directly to the spinal cord. Injections require either open surgery or a Magnetic Resonance Imaging (MRI) guided injection. Needle positioning during MRI imaging is a significant hurdle to direct spinal injection, as the small target region and interlaminar space require high positioning accuracy. **Objective:** To improve both the procedure time and positioning accuracy, an MRI guided robotic needle positioning system is developed. **Methods:** The robot uses linear piezoelectric motors to directly drive a parallel plane positioning mechanism. Feedback is provided through MRI during the orientation procedure. Both accuracy and repeatability of the robot are characterized. **Results:** This system is found to be capable of repeatability below 51 μm . Needle endpoint error is limited by imaging modality, but is validated to 156 μm . **Conclusion:** The reported robot and MRI image feedback system is capable of repeatable and accurate needle guide positioning. **Significance:** This high accuracy will result in a significant improvement to the workflow of spinal injection procedures.

Index Terms—Magnetic resonance, cellular therapeutics, piezoelectric, super-resolution.

I. INTRODUCTION

RECENT research developments have indicated the potential use of injected stem cells for treatment or mitigation of amyotrophic lateral sclerosis (ALS) and other diseases that affect the spinal cord [1]–[3]. It is critical that the cellular material is delivered directly to the site, with minimal targeting error, as cells injected into white matter are likely ineffective [4]. Two options to achieve this accuracy have been used, 1) open surgery,

Manuscript received April 11, 2020; revised July 6, 2020; accepted August 21, 2020. Date of publication September 1, 2020; date of current version February 19, 2021. This work was supported in part by the National Science Foundation under Grant 1662029, and in part by the Georgia Tech Institute for Robotics and Intelligent Machines under the FY2019 and FY2020 seed grant program. (Corresponding author: Waiman Meinhold.)

Waiman Meinhold is with the Woodruff School of Mechanical Engineering, Georgia Institute of Technology, Atlanta, GA 30332 USA (e-mail: wmeinhold@gatech.edu).

Daniel Enrique Martinez and Jun Ueda are with the Woodruff School of Mechanical Engineering, Georgia Institute of Technology.

John Oshinski is with the Department of Radiology and Imaging Sciences, Emory University.

Ai-Ping Hu is with the Intelligent Sustainable Technologies Division, Georgia Tech Research Institute.

Digital Object Identifier 10.1109/TBME.2020.3020926

in which the spinal cord and injection site are visually located by the surgeon, and 2) manual Magnetic Resonance Imaging (MRI) based needle positioning [1], [2]. The manual needle positioning method involves an iterative procedure in which the subject is imaged in the MRI scanner along with an adjustable frame. Correct targeting of the injection site requires multiple images, with the subject removed from the scanner each time so that the needle guide can be re-positioned, increasing procedure time to around 6 hours [3].

MRI based injection is preferable to open surgery, because of the ability to locate injection sites accurately and in a minimally invasive manner [3]. However, MRI compatibility places additional constraints on the design of needle positioning robots, particularly in the choice of actuators. Piezoelectric and pneumatic actuators are the two most common choices.

Pneumatic actuators have the significant advantage of large ranges of motion and simple MRI compatibility, however relatively long transmission lines are necessary and this produces complications with remote sensing and control [5]. Piezoelectric motors are capable of providing high accuracy, but often must be used with a cable drive system because of reported concerns with image artefacts [6], [7]. Remote placement of actuators, even if cable lengths are relatively short, produces additional accuracy and rigidity concerns. Many MRI based needle positioning systems exist, with applications to biopsy as well as injection of therapeutics. Broadly speaking, previously developed systems can be grouped into passive manual frames and active automated positioning systems. Manually adjustable frames have been used with a degree of success to perform intraspinal injections [3]. The system was fabricated by modifying an existing frame for neurosurgery (ClearPoint SmartFrame, MRI Interventions). While the protocol used to perform intraspinal injections in a porcine model animal was effective, it was extremely time intensive, with pre-operative planning and injection taking 2.5 hours of the total 6 hour procedure [3].

The authors are aware of only a single automated needle positioning system targeting the spinal cord as the injection site [8] although a wide range of needle positioning MR robots have been developed [6], [9]–[14]. Monfaredi discussed a large number of MR compatible robots, primarily for prostate, brain, and breast interventions [13]. The best accuracy of the reviewed robots was 23 μm , however, this system has only 3 degrees of freedom (DOF), insufficient for spinal cord applications [15]. In

addition, concerns have been raised about the Signal-to-Noise Ratio (SNR) reduction caused by the actuators when they are located close to the region of interest [7]. A reported parallel plane positioning mechanism utilizing piezoelectric ultrasonic motors demonstrated promising results, but was limited by the necessity of a cable driven actuation system, resulting in hysteresis [6].

One important benefit of a robotic needle guide in comparison with manual systems is the potential for significant reductions in injection procedure times. For example, in a previous study utilizing manual needle positioning total procedure times were around 4 hours, with trajectory planning and needle insertion taking 2.5 hours [3]. A similar study in humans where surgery to expose the spinal cord was used required a minimum of 3 hours per procedure [1]. In contrast, the prior robotic positioning study required only 10 minutes for each positioning update with a total procedure time of about 70 minutes [8].

Although the MRI sequence used during the injection procedure provides up to 1.0 mm accuracy, the design of a robot with a significantly higher accuracy will allow super resolution (SR) injection. SR algorithms require multiple sub-pixel shifted images to reconstruct a higher resolution image. One SR algorithm that has found success across a number of imaging domains is iterative back propagation [16]. Previously reported SR MRI methods demonstrated promising results by inducing sub-pixel shifts in the scanner field of view (FOV) [17], [18]. However, the mechanics of most MRI protocols preclude the effective use of this type of FOV shift method along certain axis of the image [19]. In contrast, a robot capable of producing 3 dimensional spatial shifts with precision beyond the accuracy of the scanner will enable application of these methods along any image axis. Improved resolution of robot position through super-resolution reconstruction will enable injection repeatability beyond the scanner's imaging limits. Thus, the robot design process undertaken here aims to produce a system capable of accuracy an order of magnitude greater than that of the MRI. A preliminary version of this work has been reported [20].

II. DESIGN AND CONTROL

The planned robot and visual feedback system design is shown in Fig. 1. The design and control of the robotic system is described in more detail below.

A. Mechanical Design

The robot design produced is a parallel plane structure consisting of 2 nearly identical X-Y stages which position 2 ball joints. Robot design prioritized MRI compatibility and structural rigidity to ensure accuracy and avoidance of contamination of the MRI images needed for targeting of the spinal cord. A needle guide passes through the center of each ball joint, allowing 4 Degrees of Freedom (DOF) to be controlled. the robot is shown in Fig. 2. The lower ball joint is fixed to the needle guide, while the upper ball joint allows the needle guide to slide through the center. The actuators are comprised of linear piezoelectric motors. The height between the planes is 57.5 mm, while each actuator has a range of 80 mm.

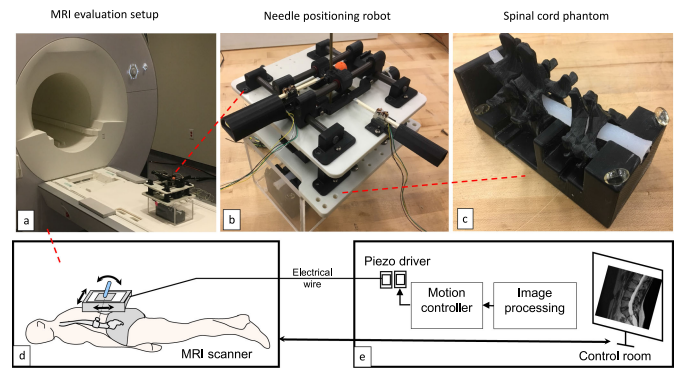


Fig. 1. MRI visual feedback schematic, (a) 3 T MRI and robot, (b) closeup of robot, (c) spinal phantom, (d) patient orientation, (e) control room diagram.

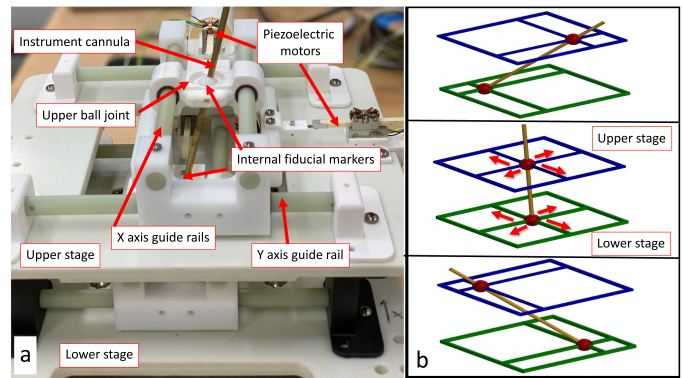


Fig. 2. Parallel plane robot, (a) robot and (b) positioning mechanism.

The y axis actuator moves the entire x axis assembly along the outer guide rods, while the x axis actuator is mounted to this assembly, and moves only the center ball joint, collar and fiducial. Each actuator is centered between the guide rods, to avoid unbalanced loads on the drive rods. Guide rods are low friction polymer, and sleeve bearings are press fit into the x assembly components and collar to decrease friction.

The only difference between the upper and lower stages is in the diameter of the needle guide hole in their respective ball joints. The lower stage has a press fit, while the upper stage is a free fit, to allow the guide to slide freely. The lower base also has additional features for mounting above the spinal cord phantom used in this study. The full robot is shown in Fig. 2(a). Four rigid brackets connect the upper and lower stages, these brackets also provide the mounting points for the lower stage y axis guide rods.

1) Specifications: The primary target for cellular therapeutics in the spinal cord is the ventral horn of the gray matter. Although the spinal cord as a whole is around 12 mm in diameter [21], the ventral horn is much smaller, with a cross sectional area near 1 mm². For this reason, accuracy of the entire robot and visual feedback system must be better than 1 mm. Time is a critical component of this system, as the primary motivation is to improve timing and accuracy of cellular therapeutic injection. The robot and feedback system should require at most 2

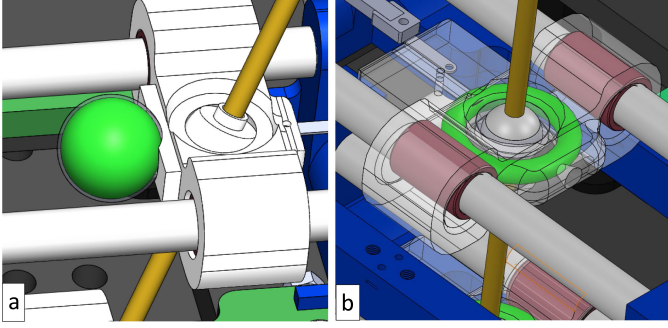


Fig. 3. Fiducial markers, vitamin E oil filled cavities shown in green, (a) spherical, co-planar with actuators and (b) toroidal, co-planar with actuators, co-axial with needle guide.

positioning updates to reach a desired trajectory, in order to keep scanner time under 15 minutes for the positioning portion of the procedure.

2) Fiducial Orientation: Because the primary materials of the robot will be transparent in MRI, only fiducial markers will be visible in the acquired images. Thus all calibration and control steps will involve the robot fiducials only. The implementation of a robot registration step, to find the transformation between robot and scanner coordinate frames is common, but can be manually intensive or technically challenging [13]. Locating fiducials on the needle axis allows robot orientation agnostic control, as the configuration is defined only by the fiducials, not necessarily the robot frame itself. By also placing the fiducials into 2 parallel planes, it is feasible to select the image slice corresponding to each plane only a single time, allowing much more rapid acquisition of images. Two different fiducial styles were used in this work, both spherical and toroidal, as shown in Fig. 3. Both fiducial styles contain internal cavities that were filled with vitamin E oil to provide MRI contrast. In the MRI imaging results presented, the spherical type was used, while the kinematic analysis presented assumes fiducials that are both co-planar with the stages, and co-axial with the needle guide, which is the toroidal fiducial shape.

3) Parallel Plane Positioning Mechanism: To avoid remote actuation and the necessity of rotary actuators for controlling rotational degrees of freedom, a parallel plane mechanism was chosen. The parallel plane positioning concept is shown in Fig. 2(b). Both the upper and lower ball joints can move independently, controlling 4 DOF of the needle guide.

The mechanism consists of 2 parallel planar stages each manipulating a ball joint. The cannula runs through these ball joints, by actuating the 4 planar axes, 4 actuated DOF are achieved, the fifth DOF, needle depth, is controlled by the surgeon inserting the needle into the cannula. The sixth DOF, needle rotation, is irrelevant for this procedure. Because the actual distance between the ball joints is dependent on the orientation, the cannula is fixed in lower joint, while the cannula slides through the center of the upper joint.

4) Materials and Fabrication: The robot described in the preceding section was fabricated from a variety of MRI safe materials using both conventional machining and fused deposition modeling (FDM) printing. FDM parts were printed in

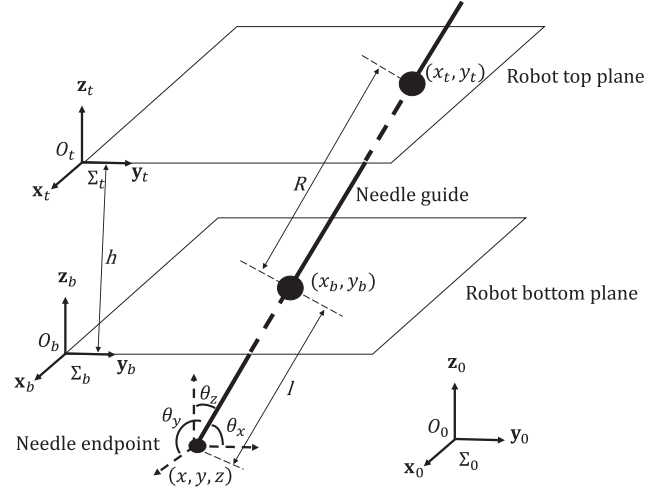


Fig. 4. Forward kinematics diagram.

acrylonitrile butadiene styrene (ABS) plastic, while machined parts consisted of acetal resin. The needle guide was cut from 4 mm brass tubing. Fasteners were titanium and nylon. The completed robot is shown in Fig. 2(a).

B. Kinematics

The forward kinematics of the robot describe the mapping of actuator positions and insertion depth to the position and orientation of the needle tip,

$$\begin{bmatrix} x \\ y \\ z \\ \theta_x \\ \theta_y \\ \theta_z \end{bmatrix} = \begin{bmatrix} -l(x_t - x_b)/R + x_b \\ -l(y_t - y_b)/R + y_b \\ -lh/R \\ \text{atan2}(y_t - y_b, h) \\ \text{atan2}(x_t - x_b, h) \\ \text{atan2}(y_t - y_b, x_t - x_b) \end{bmatrix}. \quad (1)$$

The robot's actuator positions are described by the upper x and y axis positions, x_t and y_t , the lower actuator positions x_b and y_b , and the insertion depth of the needle from the center of the lower ball joint, l , the height between planes h , is 53 mm. R used above in (1), describes the Euclidean norm of the vector between the upper and lower ball joints. The variables x , y , and z describe the position of the needle in the global fixed frame, while θ_x , θ_y , and θ_z describe the orientation of the needle in the global coordinate frame. From the robot morphology, it is clear that the latter 3, describing orientation of the needle, are not independent, as rotations about the needle axis cannot be controlled. All variables are shown in Fig. 4.

From (1), it is clear that the angular range of the robot will be determined by the travel of the upper and lower stages, as well as the distance between the two. This is reflected in Fig. 5. Physical limitations constrain the minimum value for h , the height between the planes, while larger values reduce the angular positioning capability.

1) Image Jacobian: The image Jacobian is a critical component for effective control of the parallel plane robot, as visual

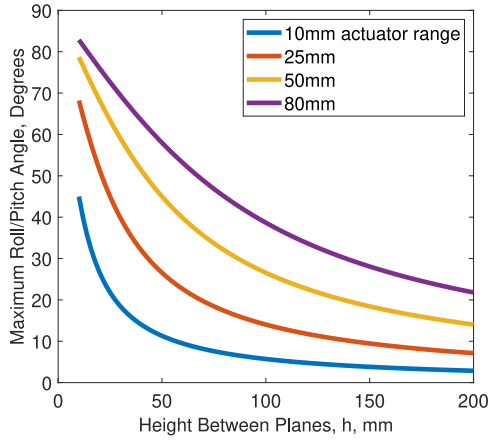


Fig. 5. Positioning range for varied actuator travel and plane distances.

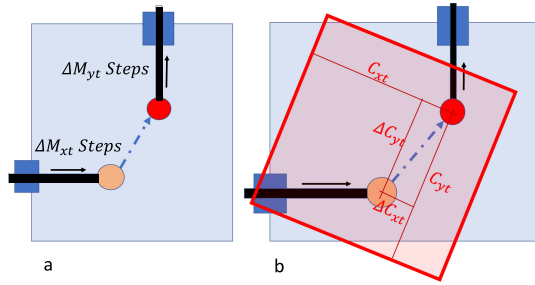


Fig. 6. Top plane positioning variables, (a) shows the robot positioning parameters, (b) shows the image plane in red and positioning variables measured via image.

servoing provides the important advantage of not being beholden to modeling error, as kinematics based control methods are. The image Jacobian relates small displacements of the actuators to motion of the fiducials

$$\mathbf{J} = \frac{\partial \mathbf{C}}{\partial \mathbf{M}^T} \quad (2)$$

where \mathbf{C} is the 4 DOF configuration of the robot fiducial markers in the image (camera) space, and \mathbf{M} represents the 4 actuator (motor) positions in the robot space, $\mathbf{C} = [C_{xt} \ C_{yt} \ C_{xb} \ C_{yb}]^T$, $\mathbf{M} = [M_{xt} \ M_{yt} \ M_{xb} \ M_{yb}]^T$. Because the fiducials are rigidly mounted to the needle guide, this Jacobian matrix also relates the actuator positions to the needle orientation. From Fig. 6 and (2), the mapping between the robot space and image space is contained within the image Jacobian, so the relative orientation of the two planes is immaterial to the positioning protocol.

2) Workspace Analysis: The workspace of the parallel plane needle positioning robot is shown in Fig. 7. The transparent surface is the reachable surface with any set of angles, while the solid surface is the reachable surface when the angle about the x axis, θ_x , is restricted to less than 15 degrees. The workspace shown was visualized by computing endpoint positions via (1) for the full range of actuator positions with needle depth of up to 10 cm. Due to the height of the robot above the patient, and observed geometry of the lumbar vertebrae, this is a reasonable restriction.

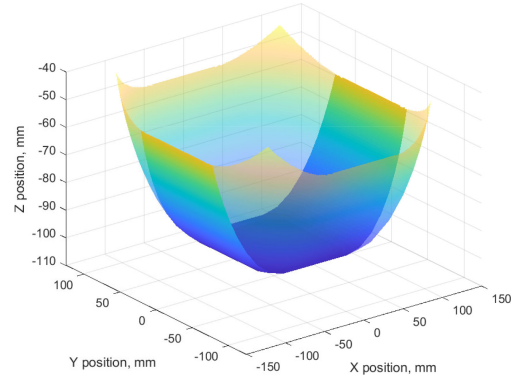


Fig. 7. Workspace of the robot, computed from the forward kinematics with a 10 cm needle length.

Algorithm 1: Imaged-Based Visual Servoing Control.

known: desired fiducial pixel coordinates, desiredFidCoords;
initialize: jog each robot axis and note corresponding change in image pixel coordinates to obtain numerical approximation of image Jacobian matrix, \mathbf{J} ; normPixelError = large value;
while normPixelError > 1 **do**
 Take MRI Image;
 pixelErrorVector = actualFidCoords – desiredFidCoords;
 normPixelError = ||pixelErrorVector||;
 Update Actuators by $-\mathbf{J}^{-1}$ pixelErrorVector;
end

3) Actuators: Positioning accuracy of the needle guide is the critical aspect of this robot. For this reason, direct drive linear motors were chosen to reduce backdrivability and backlash. Linear piezoelectric motors were chosen because of their MRI compatibility and high precision (PiezoLEGS 6 N non-magnetic, MicroMo, Clearwater, FL).

These linear motors are uniquely suited for the desired high resolution positioning, as they have a step size of 4–7 μm , consume no power when maintaining a fixed position, and are MRI compatible [22]. The ability to place these actuators inside the bore of the scanner allows a rigid link between drive rods and the robot frame, eliminating the need for gearing or a cable drive, and their associated backlash and deformation problems.

C. Visual Servoing Control

A schematic of the visual feedback system is shown in Fig. 1(e). In this paper, the visually tracked fiducials are rigidly affixed to the robot stages. Planar slices of the 3D magnetization prepared rapid gradient echo (MP-RAGE) scan (1 mm pixels, 1 mm slice thickness) shown in Fig. 9 are evaluated for the 2D pixel coordinates of the center of each of the upper and lower stage fiducials.

The desired fiducial coordinates were obtained by manually actuating the robot axes to affect a proper needle pose with respect to the spinal cord phantom and then designating the resulting coordinates as the desired ones. The image-based visual servoing control implemented is listed as Algorithm 1. This eliminates the need to use a kinematic model of the robot

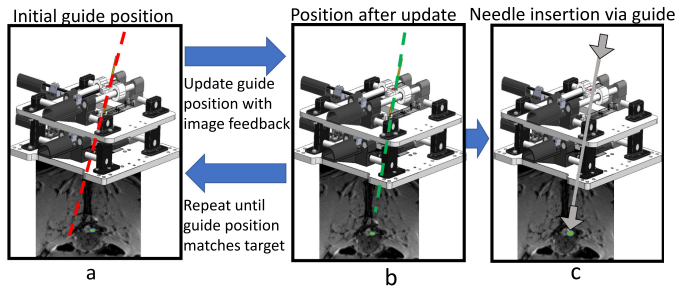


Fig. 8. Proposed injection procedure with (a) initial guide position, (b) iterative position updates and (c) insertion of needle through the robot guide.

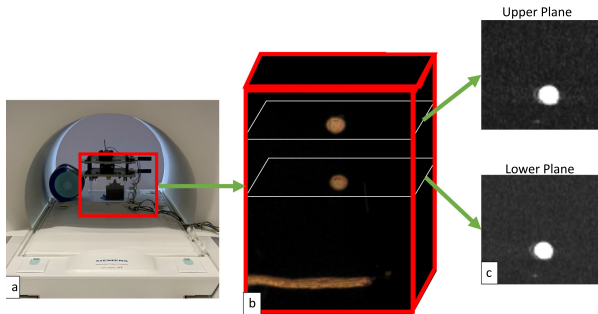


Fig. 9. MRI imaging setup, (a) robot in scanner bore, (b) 3D imaging volume, (c) upper and lower fiducial/robot planes, b & c are shown as closeups for clarity, the actual imaging volume was a 256 mm cube and included a portion of the phantom bottle shown in a.

for control. The proposed workflow is shown in Fig. 8. Error is calculated from an initial image, updates computed via the estimated Jacobian, and the procedure performed recursively until the guide reaches the target position. Once the target position is reached, a surgeon inserts the needle to the correct depth through the needle guide.

D. Phantom Construction

A phantom spinal cord and vertebrae were constructed for evaluation of the robot. CAD models from the BodyParts3D database [23] were used to create a model spinal cord and section of vertebrae. L3-L4 and C3-C4 were the chosen vertebrae, to give a range of anatomical constraints for injection sites. The vertebrae and mounting fixture were manufactured in ABS plastic with a FDM printer (Stratasys, Eden Prairie, MN). The same printer was used to create a 2-part mold for casting the spinal cord phantom. The cord was cast from a 2-part silicone that is MR-visible (DragonSkin 30, Smooth-On Inc. Macungie, PA). This phantom is shown in Fig. 1(c). The phantom was used to set target needle trajectories that avoid the vertebrae.

III. EVALUATION AND RESULTS

A. MRI Image Quality

The robot was assessed in a 3 Tesla MRI (Prisma-Fit, Siemens Healthcare, Erlangen Germany). Image quality was measured as

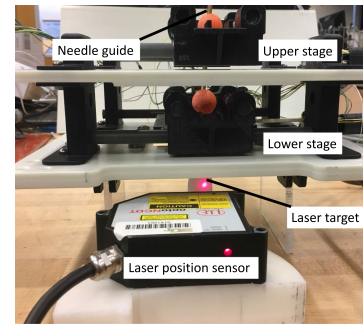


Fig. 10. Laser position sensor experimental setup.

the signal to noise ratio (SNR) reduction in a Nickel Sulfate solution cylindrical phantom. Three dimensional scans were performed under 2 different operating conditions, the first with only the phantom and RF coil (Body 18, Siemens Healthcare) in the scanner bore, and the second with the robot placed above the phantom. The imaging sequence used was the MPRAGE sequence, and scan parameters were identical throughout.

SNR was measured as the mean intensity in a 16 cm² circular region in the center of the phantom, divided by the standard deviation of an identical region in air. The calculated SNRs were 244.06 for the control image with no robot, and 230.226 for the robot. This gives a SNR reduction of 5.7% for the robot, well within the 10% reduction criteria for MRI compatibility [10]. It is likely that shielding of the actuator cables would additionally mitigate the SNR reduction observed. The SNR was not measured during actual movement of the robot, as the information from each successive image is necessary to update the robot position, and thus the positioning protocol does not require simultaneous actuation and imaging. No movement of the robot due to induced electromagnetic forces was observed, and heating of the conducting elements was not observed.

B. Repeatability and Accuracy Verification

1) 4 Axis Repeatability: The repeatability of the robot was measured with a laser triangulation sensor (optoNCDT ILD2200-20, resolution: 0.3 μ m, Micro Epsilon, Germany). The experimental setup is shown in Fig. 10. Although all 4 degrees of freedom of the robot were actuated, measurement took place at the needle endpoint along a single axis. All 4 actuators were stepped forwards and back 500 steps (\sim 2.5 mm) in each of 5 robot configurations, Actuator stepping was done 10 times for each of the 5 configurations. The mean standard deviation of these motions was 36 μ m, with a range from 19–51 μ m for each of the 5 configurations shown in Fig. 11. This shows that the open loop repeatability (3σ) of the robot is less than a sixth of the 1 mm resolution of the MRI scanner.

2) Camera Based Positioning: The results presented above demonstrated that the robot is capable of positioning repeatability at least 6 times better than the capabilities of the MRI scanner. In order to better capture the positioning capabilities of the robot, camera based visual servoing was applied. A camera placed on an aluminum bracket above the upper stage of the

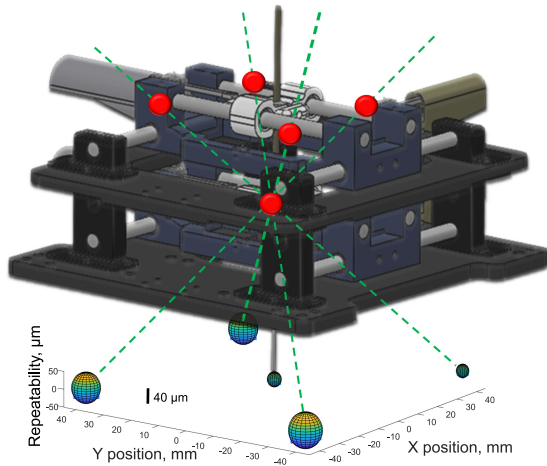


Fig. 11. Repeatability results, red dots and green lines represent the 5 evaluated robot configurations, the plotted spheres have radii equivalent to the mean standard deviation for each of the configurations.

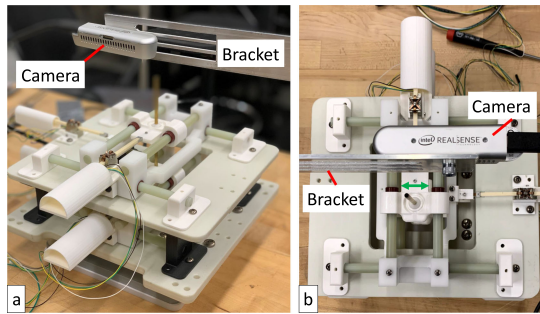


Fig. 12. Camera feedback experiments (a) Camera and mounting bracket setup and (b) Top view with calibration dimension shown in green.

robot (Intel Realsense D435 RGB-D camera) captured the planar position of the upper stage fiducial. The camera and mounting bracket are shown in Fig. 12(a). The lower stage could not be measured in all configurations, because of visual occlusion. For this reason, the position of the lower stage was fixed in the center of the workspace for the duration of the camera based experiments. The resolution of the camera was calibrated with the known 26 mm width of the collar part demarcated by a green arrow in Fig. 12(b), this resolution was $105 \mu\text{m}$ per pixel for the top fiducial.

The visual servoing method presented in section 2 C was then applied to move the upper fiducial from each of the 4 outer configurations shown in Fig. 11 to the central (vertical) configuration, and from the central configuration to each of the outer ones. Aggregate results from these 8 trials are shown in Fig. 13(a). After 9 iterations, the fiducial reached the target position, corresponding to a maximum position error of $74 \mu\text{m}$ (the diagonal of a pixel). This error is a significant improvement upon the previously developed spinal injection robot [8]. Because the upper and lower stages are both identical in construction and not rigidly coupled, maximum errors should be the same in both stages when imaging feedback is applied equally, i.e., in the MRI scanner where visual occlusion is not present.

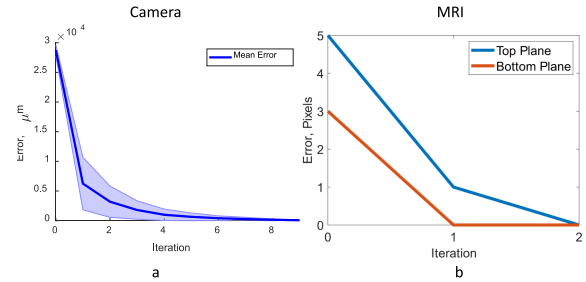


Fig. 13. Positioning results for (a) Camera based servoing and (b) MRI guided servoing.

3) MRI Positioning Feedback Experiments: The final experiment performed was a validation of the entire system in a 3 Tesla MRI. A 3D imaging protocol (MPRAGE) with a 256 mm cubic imaging volume was used. Voxel size was set to 1 mm^3 . The same visual servoing method was applied as in the above experiments, but in this case, both the upper and lower stages were actuated. The target position was set manually, prior to the beginning of imaging, and chosen so that a stainless steel rod inserted in the guide tube would pass between the vertebrae and into the phantom spinal cord. A total of 6 images were taken, with an initial image to get the target positions, 2 to compute image Jacobians, and 2 more to move both stages back to the target position. A representative image is shown in Fig. 9.

Positioning results from the last 3 images are shown in Fig. 13(b), with both the upper and lower stages reaching the target pixel after 2 updates. Targeting was confirmed by inserting the rod into the needle guide, and verifying that there was no contact with the phantom vertebrae. In this case, the absolute maximum error is 0.7 mm , or half the diagonal of a 1 mm pixel.

IV. DISCUSSION

A. Accuracy of the Robot

The robot accuracy was measured in two different experiments with two different image feedback methods. The MRI positioning experiments demonstrate that the system works as expected in the MRI environment. Only 2 position updates are required to reach a target pixel with both the upper and lower stages, indicating that the visual feedback system converges to a target within MRI resolution in a suitable time.

Camera based positioning experiments showed that if the imaging feedback is provided at a higher resolution, the robot is capable of higher accuracy than the MRI, with 9 updates producing positioning with a maximum error of only $74 \mu\text{m}$. In this case, accuracy of the robot is limited by imaging feedback, because the target pixel was reached in all 8 of the trials.

The most accurate measurements of the robot's repeatability were performed with the laser triangulation sensor. In this case, the needle guide position was measured directly, instead of the upper and lower stages. This measurement then takes into account possible errors in positioning due to relative displacement of the needle guide and fiducials during movement. The repeatability tests showed that even with open loop operation of

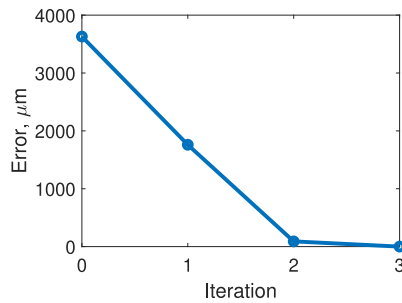


Fig. 14. Positioning results with laser position feedback.

the actuators, the positioning repeatability is quite good, with a maximum standard deviation of only $51 \mu\text{m}$, about 1/20 of the pixel size produced by the MRI. The ability of the robot to repeatably produce positions with higher accuracy than a single MRI pixel motivates the future development of image reconstruction methods to provide super-resolution positioning in the scanner environment to surpass the current limitations created by the MRI scanner resolution.

Although the best available image feedback system, the RGB camera, had a resolution of $105 \mu\text{m}$, the laser repeatability measurements indicated that higher accuracy positioning is likely possible. For this reason, the laser position sensor used to measure positioning repeatability was applied in a simple linear feedback positioning task. The robot was set in the vertical configuration at the center of the workspace, with the laser position sensor measuring the needle endpoint. A single actuator was then moved to an arbitrary position, ensuring that the endpoint stayed within the range of the laser sensor. From there, a basic linear feedback method was applied, with the results shown in Fig. 14. The limitation again appears to be the resolution of the laser sensor (measurement resolution $9.4 \mu\text{m}$), and not the accuracy of the feedback method or robot itself.

B. Image and Positioning Time

Imaging time is the most significant contributor to overall procedure time, with each image taking 6.25 minutes to acquire. Robot actuation is comparatively short, 6 s and 4 s respectively for the updates shown in Fig. 13(b). This is comparable with a previously developed, but less accurate, spinal injection robot [8], and much faster than manual positioning methods and open surgery. The 3D sequence used is clearly excessive for the positioning requirements, as after target fiducial locations are known only the two planes containing the fiducials are necessary for computation of actuator updates. By selecting only these 2D images, imaging time could be significantly improved, with the full 3D volume only necessary for targeting and validation.

C. Visual Servoing and Target Selection

The visual servoing-based positioning accuracy results presented in this paper were based on fiducials affixed to each of the two robot stages, with their desired coordinates being obtained manually. Future work will seek to locate the fiducials co-axially

with the needle. Desired coordinates will be computed based on a vector line drawn by a skilled practitioner (e.g., a surgeon) on the 3D MRI reconstruction. These changes will generalize the utility of the described system, remove the need for a priori information that may be difficult to ascertain in practice, and more closely align with clinical protocol. Although segmentation of the spinal cord from MRI images is possible [24], the sensitive nature of the procedure encourages target selection by a trained clinician.

D. Clinical Considerations

While the work presented here demonstrated the high precision and accuracy of a novel MRI guided needle positioning robot and associated visual feedback method, certain clinical concerns remain. Patient mounting was not addressed in this work, but several potential methods have previously been reported for other injection robots. The manually adjustable MRI guided frame used for this procedure previously utilized lamina screws rostral and caudal to the injection target [3]. This approach is feasible for the new robot reported here. In addition, interaction between the mechanism and tissue may induce small inaccuracies in positioning. In particular, respiration and the force required to puncture the skin of the patient may both induce deflection or motion of the robot. Because the targeted injection site is in the spine, the patient will be prone in the scanner bore, with the robot mounted to the patient's back, this means that respiration should not cause major positioning errors, but this needs to be verified with (non-invasive) human subject trials. A human cadaver study found that the maximum force required to perform a lumbar puncture with an 18 gauge needle was under 5 N [25]. It is important to note that with the proposed workflow, there should be very small forces along the needle guide axis, as the robot guides the needle, but does not independently perform the insertion.

V. CONCLUSION

This paper presented a new MRI guided needle guide positioning robot for spinal cord injection. To maximize the effectiveness of cellular therapeutics, it is critical that targeting error be minimized during injections. The use of a parallel plane positioning mechanism with direct actuation from linear piezoelectric motors produces a robot with linear positioning repeatability 6 times better than MRI resolution ($3\sigma = 153 \mu\text{m}$). The addition of positioning feedback allows accuracy up to the resolution of the imaging system, $74 \mu\text{m}$ in the case of an RGB camera, and 0.7 mm in the case of the MRI scanner.

ACKNOWLEDGMENT

The authors would like to thank Nytavia Wallace and Vishwadeep Ahluwalia of the GSU/GT Center for Advanced Brain Imaging for their essential help in carrying out the MRI portions of this work. The authors would also like to thank Alex Zabaldo, Jae Kim and Ishrat Arora for their assistance in designing and fabricating the robot and phantom.

REFERENCES

- [1] Glass *et al.*, "Lumbar intraspinal injection of neural stem cells in patients with amyotrophic lateral sclerosis: Results of a phase I trial in 12 patients," *Stem Cells*, vol. 30, no. 6, pp. 1144–1151, Jun. 2012.
- [2] Mazzini *et al.*, "Stem cell therapy in amyotrophic lateral sclerosis: A methodological approach in humans," *Amyotrophic Lateral Sclerosis Other Motor Neuron Disorders*, vol. 4, no. 3, pp. 158–161, 2003.
- [3] Lamanna *et al.*, "Magnetic resonance imaging-guided transplantation of neural stem cells into the porcine spinal cord," *Stereotactic Functional Neurosurg.*, vol. 95, no. 1, pp. 60–68, 2017.
- [4] Janowski *et al.*, "Survival of neural progenitors allografted into the CNS of immunocompetent recipients is highly dependent on transplantation site," *Cell Transplantation*, vol. 23, no. 2, pp. 253–262, 2014.
- [5] Turkseven and Ueda, "An asymptotically stable pressure observer based on load and displacement sensing for pneumatic actuators with long transmission lines," *IEEE/ASME Trans. Mechatronics*, vol. 22, no. 2, pp. 681–692, Apr. 2016.
- [6] Hungr *et al.*, "Design and validation of a CT-and MRI-guided robot for percutaneous needle procedures," *IEEE Trans. Robot.*, vol. 32, no. 4, pp. 973–987, Aug. 2016.
- [7] Fischer *et al.*, "MRI compatibility of robot actuation techniques—a comparative study," in *Proc. Int. Conf. Med. Image Comput. Comput.-Assisted Intervention*, 2008, pp. 509–517.
- [8] Squires *et al.*, "Spinobot: An MRI-guided needle positioning system for spinal cellular therapeutics," *Ann. Biomed. Eng.*, vol. 46, no. 3, pp. 475–487, 2018.
- [9] Hempel *et al.*, "An MRI-compatible surgical robot for precise radiological interventions," *Comput. Aided Surg.*, vol. 8, no. 4, pp. 180–191, 2003.
- [10] Chinzei *et al.*, "Mr compatible surgical assist robot: System integration and preliminary feasibility study," in *Proc. Int. Conf. Med. Image Comput. Comput.-Assisted Intervention*, 2000, pp. 921–930.
- [11] Melzer *et al.*, "Innomotion for percutaneous image-guided interventions," *IEEE Eng. Med. Biol. Mag.*, vol. 27, no. 3, pp. 66–73, May/Jun. 2008.
- [12] Patel *et al.*, "Preclinical evaluation of an integrated robotic system for magnetic resonance imaging guided shoulder arthrography," *J. Med. Imag.*, vol. 6, no. 2, 2019, Art. no. 025006.
- [13] Monfaredi *et al.*, "MRI robots for needle-based interventions: Systems and technology," *Ann. Biomed. Eng.*, vol. 46, no. 10, pp. 1479–1497, 2018.
- [14] Comber *et al.*, "Design and control of an magnetic resonance compatible precision pneumatic active cannula robot," *J. Med. Devices*, vol. 8, no. 1, 2014, Art. no. 011003.
- [15] Yiallouras *et al.*, "Three-axis MR-conditional robot for high-intensity focused ultrasound for treating prostate diseases transrectally," *J. Therapeutic Ultrasound*, vol. 3, no. 1, 2015, Art. no. 2.
- [16] Irani *et al.*, "Motion analysis for image enhancement: Resolution, occlusion, and transparency," *J. Vis. Commun. Image Representation*, vol. 4, no. 4, pp. 324–335, 1993.
- [17] Peled and Yeshurun, "Superresolution in MRI: Application to human white matter fiber tract visualization by diffusion tensor imaging," *Magn. Reson. Med.: Official J. Int. Soc. Magn. Reson. Med.*, vol. 45, no. 1, pp. 29–35, 2001.
- [18] Greenspan *et al.*, "MRI inter-slice reconstruction using super-resolution," *Magn. Reson. Imag.*, vol. 20, no. 5, pp. 437–446, 2002.
- [19] Scheffler, "Superresolution in MRI?" *Magn. Reson. Med.: Official J. Int. Soc. Magn. Reson. Med.*, vol. 48, no. 2, pp. 408–408, 2002.
- [20] Meinhold *et al.*, "Design and fabrication of an automated spinal precision injection robot," presented at Biomedical Engineering Society Annual Meeting, 2019.
- [21] Frostell *et al.*, "A review of the segmental diameter of the healthy human spinal cord," *Frontiers Neurol.*, vol. 7, 2016, Art. no. 238.
- [22] PiezoMotor Staff, *Piezo LEGS Linear 6N*, PiezoMotor, 2019.
- [23] Mitsuhashi *et al.*, "Bodyparts3d: 3d structure database for anatomical concepts," *Nucleic Acids Res.*, vol. 37, pp. D782–D785, 2009.
- [24] De Leener *et al.*, "Robust, accurate and fast automatic segmentation of the spinal cord," *Neuroimage*, vol. 98, pp. 528–536, 2014.
- [25] Ambastha *et al.*, "Comparison of force required for lumbar puncture with different gauges of spinal needle using fiber Bragg grating force device," *IEEE Sensors J.*, vol. 18, no. 19, pp. 8028–8033, Oct. 2018.